Chapter 2

Experimental procedure and characterization techniques

In the study of functional materials, understanding physical properties is essential to determine their potential applications. Therefore, a comprehensive experimental investigation is necessary to explore the underlying structural dynamics and correlate them with the observed macroscopic properties. This chapter provides an overview of the experimental procedures and characterization techniques used to investigate the sodium niobate-based solid solution, i.e., NN-xBCT. Various structural, spectroscopic, and electrical measurement techniques were employed to probe the structural ordering at multiple length scales, detect phase transitions, and evaluate the dielectric and ferroelectric properties of the synthesized samples.

2.1 Sample synthesis

In this thesis, we synthesized powder samples of various compositions. The properties of these powder samples significantly influence subsequent processing steps, including the formation of powders into cylindrical pellets and the sintering process, which ultimately

determines the desired microstructure. There are a number of different processing routes for preparing powder ceramic samples *viz.,* solid-state reaction method, sol-gel method, hydrothermal method, etc. The selection of a preparation method is influenced by factors such as production cost and the ability of the method to achieve a specific set of desired characteristics. We employed the conventional solid-state reaction method for the preparation of powder samples, as it is a simple and cost-effective approach for producing ceramic samples.

2.1.1 Solid-state reaction method

The solid-state reaction method is a widely used technique for synthesizing polycrystalline materials using solid reactants [212]. In this method, chemical reactions between solid starting materials (such as oxides and carbonates) are commonly used to produce oxides like titanates, ferrites, and silicates. These reactions involving the decomposition of solids or chemical interactions between them are known as calcination. The solid-state reaction method begins with the mixing of raw materials according to their chemical stoichiometry. Mixing can be carried out manually using an agate mortar and pestle or mechanically using a ball mill. In this study, we opted for the latter method to mix and grind the raw materials. For ball milling, we employed the wet mixing method, where the raw powders were placed in a zirconia jar along with zirconia balls and an ethanol medium. The mixing was then carried out using a planetary ball mill (Retsch model PM 200). Afterwards, the resulting slurry is dried, and the milled powders are separated from the zirconia balls. The powders are then subjected to heat treatments. The mixed powders were placed in alumina crucibles and calcined at elevated temperatures using a programmable muffle furnace. After calcination, the powders were mixed with 2 wt% polyvinyl alcohol (PVA), which served as a binder to enhance the mechanical strength of pellets. The blended mixture was then pelletized into disc-shaped samples using a hydraulic press. Subsequently, the pellets

underwent a sintering process in a programmable muffle furnace at a temperature higher than the calcination temperature to achieve the desired densification and microstructure. The instruments employed for the synthesis of samples using the solid-state reaction method are illustrated in Fig. 2.1. Upon successful synthesis, the samples were subjected to a wide range of characterization techniques, as outlined below.

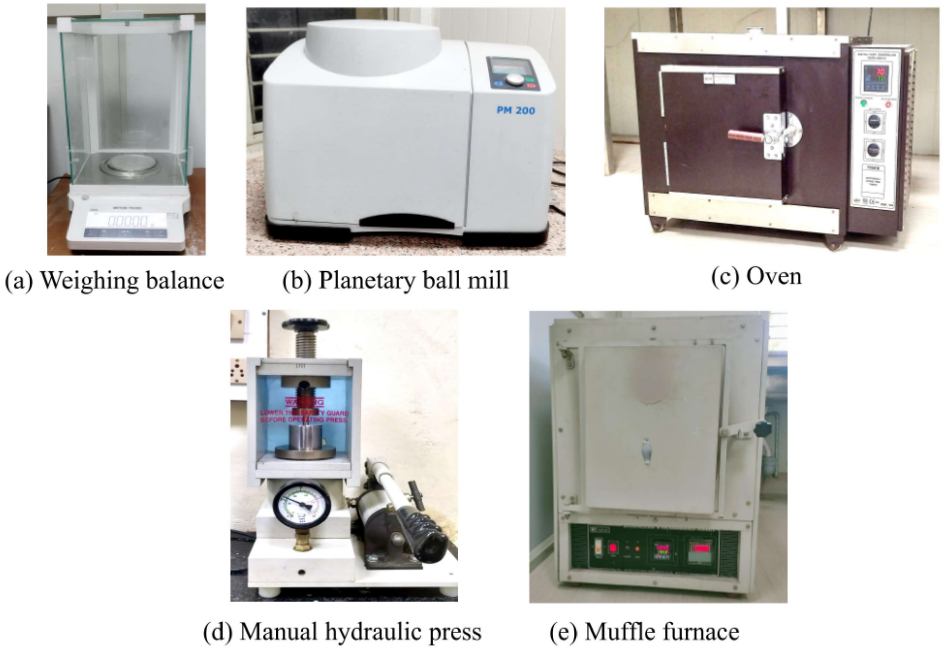

Fig. 2.1 The instruments used in the synthesis of samples via the solid-state reaction method.

2.2 Characterization techniques

Crystallographic symmetry of the material is an important factor influencing various physical properties such as ferroelectricity, piezoelectricity, optical properties, and so on. Therefore, it is important to identify the crystal symmetry of functional materials at multiple length scales using suitable methods such as X-ray diffraction, Vibrational spectroscopy, Total scattering analysis, etc. Furthermore, it is essential to supplement the structural analysis with physical property measurements to establish a correlation between

the crystal structure and its properties. This approach enables us to assess the suitability of material for a range of applications, including ferroelectric memory devices, energy storage systems, sensor and actuator technologies. The following sections provide an overview of various structural analysis and electrical characterization techniques.

2.2.1 X-ray diffraction method

As mentioned earlier, the crystal structure plays a pivotal role in defining the physical properties of a material, with most properties being closely linked to its symmetry. Hence, determining the crystal structure across different length scales is essential. X-ray diffraction (XRD) serves as a fundamental technique for examining the average structure (up to a few hundred unit cells) of materials. This is because the wavelength of X-rays is of the order of the distance between the atomic planes, which act as diffraction slits. X-ray diffraction (XRD) is based on Bragg's law, formulated by Lawrence Bragg and his father, William Bragg, in 1913. They suggested that crystals can be visualized as having planes of electron clouds associated with the atoms.

When X-rays with wavelengths similar to the interplanar spacing of crystal planes interact with a crystalline material, they undergo diffraction due to the ordered arrangement of atoms. The scattered waves emitted from atoms positioned at various locations can interfere constructively or destructively depending on the direction. Maximum intensity is observed when the following geometric condition is met (see 2.2) [213].

$$2d_{hkl}sin\theta = \lambda \quad (Bragg's\ law) \tag{2.1}$$

Here, d_{hkl} denotes the interplanar spacing for a specific family of planes characterized by the Miller indices h,k,l, λ represents the wavelength of the X-ray, and θ is the Bragg an-

gle, which is the angle between the incident ray and the crystal plane. Consequently, 2θ is the angle between the incident beam and the diffracted beam (see Fig. 2.2).

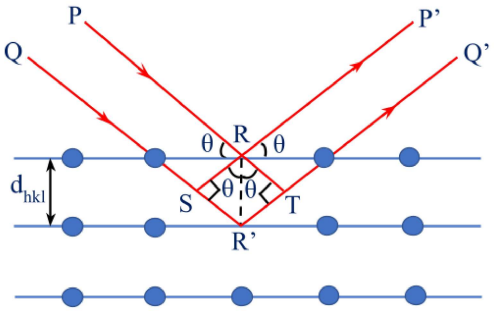

Fig. 2.2 Representation of X-ray diffraction by a crystal.

To analyse the crystallographic phase and purity of the synthesized ceramics, we have used two sources (i) High-resolution Laboratory X-ray diffraction (HRXRD): This is a 9kW rotating anode-based Rigaku SmartLab high-resolution X-ray diffractometer (see Fig.2.3), operated in Bragg–Brentano geometry. The X-ray diffraction data have been collected over the 2θ range 20^0 to 120^0 with a step size of 0.02, using Cu-$K_{\alpha 1}$ (1.54059 Å) radiation. The data were recorded in a continuous scan mode. (ii) Synchrotron X-ray diffraction (SXRD): The Synchrotron X-ray Diffraction data collected using Beamline 28-ID-2 (X-ray Powder Diffraction, XPD) at NSLS2 (National Synchrotron Light Source) at Brookhaven National Laboratory (Fig. 2.4).

It is important to note that both Synchrotron and laboratory X-ray diffraction (XRD) are essential tools for structural analysis, but they differ in key aspects. Laboratory XRD uses conventional X-ray tubes with fixed wavelengths, providing sufficient resolution for routine material characterization. In contrast, synchrotron XRD, generated from large particle accelerators, offers extremely bright, tunable X-rays with higher resolution and sensitivity, making it ideal for studying complex materials, weak reflections, and phase transitions. While laboratory XRD is cost-effective and widely accessible, synchrotron XRD enables experiments under extreme conditions(high pressure/ temperature/ electric field). Researchers often use both techniques together for comprehensive material analysis.

In order to fix the crystallographic structure of the various synthesized ceramics, we have

performed the Rietveld refinements of the X-ray diffraction patterns using the FULLPROF package [214].

2.2.2 Rietveld Refinement

Rietveld refinement is a robust and extensively used method for analyzing X-ray and neutron diffraction data, particularly for polycrystalline materials. It was first introduced by Hugo Rietveld in 1969 for the analysis of neutron diffraction data and was later adapted for X-ray diffraction. The primary goal of this technique is to extract detailed crystallographic information by fitting a calculated diffraction pattern to the experimentally observed data using a least-squares optimization procedure [215]. Unlike conventional diffraction analysis methods that focus only on the positions and intensities of individual diffraction peaks, Rietveld refinement utilizes the entire diffraction pattern for more comprehensive analysis. Refining multiple structural parameters, including lattice constants, atomic positions, site occupancies, and thermal vibrations, provides a deeper understanding of the crystal structure. This makes it particularly effective for investigating complex materials, including those exhibiting structural phase transitions or containing mixed phases. In this study, Rietveld refinement was performed to analyze the crystal structures of sodium niobate-based ceramics. The method enabled us to precisely determine the symmetry, lattice distortions, and atomic displacements within the material

Fig. 2.3 Rigaku SmartLab high-resolution X-ray diffractometer.

across various temperatures, contributing significantly to our understanding of its phase transitions and structure-property relationships.

The Rietveld refinement technique is based on a least-squares approach that minimizes the difference between the experimental diffraction data and the theoretically calculated pattern. The diffraction data consists of the observed intensity values at specific diffraction angles (2θ), denoted as I_{obs}. The calculated intensity values (I_{calc}) are generated using a structural model that includes atomic positions, unit cell parameters, and peak shape functions [215]. The difference between the observed and calculated intensities is quantified by a residual value, which is minimized during the refinement process. The minimized sum of squared residuals (S) is expressed as follows [216]:

$$S = \sum w_i \left(y_{\text{obs},i} - y_{\text{calc},i}\right)^2$$

Where:

- $w_i = \frac{1}{y_{\text{obs},i}}$ represents the weight assigned to each data point based on its uncertainty.
- $y_{\text{obs},i}$ and $y_{\text{calc},i}$ denote the observed and calculated intensities at the i^{th} data point.

During the Rietveld refinement, several structural and instrumental parameters are adjusted to minimize the discrepancy between experimental and calculated patterns. These parameters can be broadly classified as follows:

- **Lattice Parameters:** Define the size and shape of the unit cell, including parameters such as a, b, c, and angles α, β, and γ.
- **Atomic Positions:** Fractional coordinates of atoms within the unit cell, represented as (x, y, z).
- **Occupancy Factors:** Probability of finding a particular atom at a specific site, often used in substitutional or disordered systems.

- **Thermal Parameters:** Described by Debye-Waller factors (B), representing atomic vibrations around equilibrium positions.
- **Profile Parameters:** Peak shape and width parameters are refined to model broadening effects.

The choice of the peak shape function is crucial for accurately modelling diffraction patterns [216]. Diffraction peaks are often subject to broadening due to instrumental factors, crystallite size, and microstrain. The most commonly used peak-shape functions include is pseudo-Voigt function, which is a combination of Gaussian and Lorentzian functions : The Pseudo-Voigt function is given by:

$$P(x) = \eta L(x) + (1-\eta)G(x)$$

Where:

- $L(x)$ and $G(x)$ represent Lorentzian and Gaussian functions, respectively.
- η is the mixing parameter.

The accuracy of the refined structural model is evaluated using various goodness-of-fit parameters. To assess the quality of a Rietveld refinement, several statistical parameters are used [216]:

1. **Weighted profile R-factor (R_{wp})**

$$R_{wp} = \sqrt{\frac{\sum w_i \left(y_{\text{obs},i} - y_{\text{calc},i}\right)^2}{\sum w_i y_{\text{obs},i}^2}}$$

2. **Expected R-factor (R_{exp})**

$$R_{exp} = \sqrt{\frac{N-P}{\sum w_i y_{\text{obs},i}^2}}$$

Where N is the number of data points and P is the number of refined parameters.

3. **Goodness of fit (χ^2)**

$$\chi^2 = \frac{R_{wp}^2}{R_{exp}^2}$$

A χ^2 value close to 1 indicates a good fit, suggesting that the model accurately describes the experimental data. Although these parameters can be used to judge the quality of the refinement, it is important to avoid over-interpreting them. The most crucial criterion to judge the quality of Rietveld refinement is the fitting between the observed and calculated patterns and the chemical sense of the structural model obtained after the best fit [217].

In our study, we have extensively used Rietveld refinement to analyze sodium niobate-based ceramics, shedding light on their structural evolution with temperature/composition. These insights contribute significantly to understanding the structure-property relationships and optimizing materials for practical applications. Several software packages are available for performing Rietveld refinement, *viz.,* FullProf, GSAS-II, TOPAS, JANA etc. In this thesis work, we have used FullProf for performing Rietveld refinement due to its versatility and accuracy in analyzing polycrystalline diffraction data.

2.2.3 Pair Distribution Function (PDF) analysis

Many functional materials that exhibit fascinating properties such as high electromechanical response, high dielectric response, colossal magnetoresistivity, etc., exhibit distinct atomic ordering at long and short ranges, which are critical for their performance [218]. While diffraction techniques are commonly used to determine the long-range structure of polycrystalline ceramics, they are insufficient in capturing structural information in cases where short-range order differs from long-range order. Elemental substitutions at the A and/or B sites can lead to deviations in the structure at short ranges from that

of long ranges [219]. These local-scale irregularities often influence material properties in ways that cannot be fully explained by the long-range structure alone. Therefore, it is important to quantify the local structural distortions via suitable techniques. The pair distribution function (PDF) analysis (or Total scattering analysis) is an effective approach for investigating the atomic-scale (local) structure of materials derived from X-ray and neutron total scattering data [218]. While it has traditionally been employed to investigate amorphous materials and liquids, its application has later expanded to include crystalline materials, particularly perovskite-based dielectrics and ferroelectrics [220, 221, 222, 223]. Total scattering measurements account for Bragg diffraction (long-range structure), elastic diffuse scattering (local structure), and inelastic scattering. The diffuse scattering contains vital information about local structural disorder in materials. The Pair Distribution Function (PDF) is typically represented by the reduced pair distribution function $G(r)$, which is a one-dimensional function of radial distance r [218]. This function is derived by applying a Fourier transform to the total scattering structure function $S(Q)$ and expressed by the following relation [218]:

Fig. 2.4 The National Synchrotron Light Source II (NSLS-II), Brookhaven National Lab, US

$$G(r) = 4\pi r\left(\rho(r) - \rho_0\right) = \frac{2}{\pi}\int_0^{\infty} Q\left(S(Q) - 1\right)\sin(Qr)\,dQ \tag{2.2}$$

Here, $\rho(r)$ is the atomic pair density function, ρ_0 is the number density of atoms in the material, Q is the magnitude of the scattering vector (or momentum transfer), and r is the interatomic distance. In equation 2.2, the integration over Q ideally extends to infinity.

However, in practical scenarios, access to an infinite Q-range is not possible. Therefore, a finite upper limit $Q_{\max}$ is used which is defined as:

$$Q_{\max} \leq \frac{4\pi \sin\theta_{\max}}{\lambda}$$

where $\theta_{\max}$ is the maximum incident angle of the beam and λ is the wavelength of the radiation. The truncation of the integration at $Q_{\max}$ introduces termination effects, which can cause artefacts in the pair distribution function (PDF) analysis. To obtain an accurate $S(Q)$ from the raw total scattering patterns, meticulous attention is required. The proper $S(Q)$ is achieved only after applying necessary corrections for absorption, multiple scattering, and incoherent scattering, along with the subtraction of sample-independent background contributions.

A lot of structural information can be obtained from the peaks in the atomic Pair distribution function $G(r)$. The three most important information that can be obtained from atomic PDF peaks are: **(i)** peak position gives the idea of atom-pair separations (bond-lengths), **(ii)** peak integrated intensity tells about the coordination number of the corresponding atomic pair, and **(iii)** peak width reflects the atomic probability distribution. For a detailed analysis of local structural symmetry, the experimental PDF can be fitted with the tentative structural models using real-space PDF refinement.

In this thesis work, the X-ray PDF was collected using Beamline 28-ID-2 (X-ray Powder Diffraction, XPD) at NSLS2 (National Synchrotron Light Source) at Brookhaven National Laboratory. Additionally, high-Q data for an empty borosilicate capillary were collected for background subtraction, which is necessary for converting the raw diffraction data into the total scattering structure function S(Q). The S(Q) was derived from high-Q data after performing standard normalization and background corrections on the raw scattering data using the PDFgetX3 program [224]. The structure refinement of the experimental atomic PDF was carried out in the direct space using the program PDFgui [225].

2.2.4 Raman Spectroscopy

Raman spectroscopy is a non-destructive and powerful technique used for probing structural distortions in perovskites at short ranges [226]. It provides crucial information about the local structure, phase transitions, and lattice dynamics, making it an essential tool for studying ferroelectrics and relaxor materials. The interaction of light with the phonons in the material results in inelastically scattered light, leading to a characteristic Raman spectrum.

When light interacts with a material, most of it undergoes elastic scattering (Rayleigh scattering). However, a small fraction of light undergoes inelastic scattering, known as Raman scattering, where the energy of the scattered photons changes due to interactions with the vibrational modes of the crystal lattice. The energy shift in the scattered light corresponds to the vibrational energies of the material, providing a unique fingerprint of the material's structure. The frequency shift ($\Delta\nu$) observed in a Raman spectrum is given by the relation:

$$\Delta\nu = \nu_i - \nu_s$$

where ν_i is the frequency of the incident light and ν_s is the frequency of the scattered light. If $\nu_s < \nu_i$, it is called a Stokes shift, and if $\nu_s > \nu_i$, it is called an anti-Stokes shift. The Raman effect was experimentally observed in 1928 by an Indian scientist, Sir C. V. Raman. He was awarded the Nobel Prize in 1930 for this discovery.

The Raman activity of a particular vibrational mode is determined by the symmetry of the crystalline lattice. For a mode to be Raman active, it must induce a change in the polarizability of the material [227]. The selection rules for Raman modes are derived using group theory, considering the point group symmetry of the crystal. Moreover, in perovskite-based materials, symmetry breaking caused by local structural distortions (polar nanoregions (PNRs)) can lead to the activation of otherwise forbidden Raman modes, e.g., polar rhombohedral ordering in a non-polar matrix.

Fig. 2.5 WITec Raman Microscope alpha300R

In our study, the room temperature Raman spectra have been collected using the alpha300 RAS system from WITec with an excitation source of a 532 nm green laser (see Fig. 2.5). The variable temperature Raman spectra were acquired using a Horiba LabRAM HR Raman spectrometer with an Olympus BX41 microscope attachment. An excitation wavelength of 514.5 nm from a Lexel Model-95 argon ion laser was used. The samples were placed in a Linkam THMS600 microscope stage for variable temperature Raman measurements. The laser beam was focused onto the sample using a 50x LWD objective (N.A.=0.50), and the backscattered light was dispersed via a 600 lines/mm grating onto a liquid nitrogen-cooled CCD detector. The data were acquired using LabSpec v5 software. The laser power at the sample was approximately 0.4 mW. This value was checked to verify that no local heating effects from the laser beam occurred. We have used a Lorentzian function to fit the Raman pattern. The key parameters extracted from Raman spectra after the fitting are:

- **Peak Position:** Shifts in the peak position are indicative of changes in lattice dynamics, often associated with phase transitions.
- **Full Width at Half Maximum (FWHM):** The FWHM corresponding to the Raman mode provides information about the phonon width and structural disorder within the material. Broadened peaks typically suggest a higher degree of structural disorder.
- **Intensity:** Sharp changes in the intensity of Raman modes can be linked with a structural phase transition.

The Raman spectra of perovskites (ABO_3) primarily arise from two main factors:

1. The motion of the A-site cation relative to the BO_6 octahedra.
2. The internal vibrational modes of the BO_6 octahedra, which include:
   (a) Stretching vibrations of B–O bonds.
   (b) Bending vibrations of O–B–O bonds.

Based on these contributions, the Raman spectra of perovskite-based materials can be classified into three distinct regions (according to their wavenumber ($\bar{\nu}$)):

- $\bar{\nu} \lesssim 150$ **cm**$^{-1}$**:** This region is associated with the translational motion of the A-site cation with respect to the BO_6 octahedra.
- 150 **cm**$^{-1} \lesssim \bar{\nu} \lesssim 450$ **cm**$^{-1}$**:** This range corresponds to the bending vibrations of the O–B–O bonds.
- 450 **cm**$^{-1} \lesssim \bar{\nu} \lesssim 850$ **cm**$^{-1}$**:** The stretching vibrations of B–O bonds dominate in this region.

In this thesis work, temperature(or composition) dependent Raman measurements were employed to investigate the structural phase transitions, detect polar nanoregions, and

analyze the role of lattice vibrations in the structural phase transitions. These insights contribute to establishing a strong correlation between the crystal structure and functional properties of the synthesized materials.

2.2.5 Dielectric Measurements

Fig. 2.6 LCR meter along with variable temperature stage for dielectric measurements.

Dielectric properties are essential characteristics of materials that describe their ability to store and dissipate electrical energy [4]. These properties are particularly significant in functional ceramics such as normal ferroelectrics and relaxors, which exhibit strong coupling between their structural, electrical, and mechanical behaviours. The investigation of dielectric properties provides valuable insights into phase transitions, polarization mechanisms, and the dynamic behaviour of dipoles within the material. In this study, the temperature and frequency dependence of the dielectric constant (ε_r) and dielectric loss ($\tan\delta$) were systematically measured to explore the structural and ferroelectric transitions

in sodium niobate-based ceramics. These measurements were performed using an LCR meter in conjunction with a temperature-controlled environment.

The dielectric constant, also referred to as the relative permittivity (ε_r), quantifies a material's ability to store electrical energy when subjected to an external electric field [4]. It is defined as:

$$\varepsilon_r = \frac{C}{C_0}$$

Where:

- C is the capacitance of the material.
- C_0 is the capacitance of a vacuum capacitor with the same geometry.

The dielectric loss tangent ($\tan\delta$) represents the energy dissipation within the material due to the lag between polarization and the applied electric field. It is expressed as:

$$\tan\delta = \frac{\varepsilon''}{\varepsilon'}$$

Where:

- ε' is the real part of the dielectric constant, representing stored energy.
- ε'' is the imaginary part, associated with energy dissipation.

Dielectric measurements are widely used to study phase transitions, particularly in ferroelectric and relaxor materials. A distinct anomaly in the dielectric permittivity, typically a peak, is commonly observed at the phase transition temperature. Further, unlike the conventional ferroelectrics, the anomalies of the dielectric spectra of relaxors do not represent a long-range phase transition phenomenon. For relaxors, the peak is often broad and frequency-dependent due to the presence of polar nanoregions (PNRs) and dynamic

polarization fluctuations. A high dielectric constant and low dielectric loss are often desirable for applications in multi-layer ceramic capacitors and High-frequency communication devices.

In the present study, the dielectric measurements were carried out using a precision LCR meter (e.g., Keysight E4980AL) with a frequency range from 1 kHz to 1 MHz (see Fig. 2.6). The heating rate was kept at 1.5 °C /min to avoid superheating and supercooling effects. The sintered samples were polished to obtain parallel surfaces, and silver paste was applied to form conductive electrodes. The electrodes were dried and cured to ensure good electrical contact. Further, the samples were mounted in a variable temperature stage with temperature control in the range of 100 K to 600 K. Afterwards, dielectric data were collected over a wide range of frequencies using the LCR meter. Both the real and imaginary parts of the dielectric permittivity were recorded as a function of temperature and frequency.

2.2.6 Polarization vs. Electric field (PE) hysteresis loop measurements

Ferroelectric materials are characterized by their spontaneous polarization, which can be reversed under the influence of an external electric field. A key feature of ferroelectric materials is their non-linear polarization response, represented by a hysteresis loop in a plot of polarization (P) versus the applied electric field (E) [17]. The measurement of hysteresis loops is essential for evaluating the ferroelectric properties of materials, providing critical information about remnant polarization, coercive field, saturation polarization, and energy storage capability. These parameters are significant for applications in memory devices, sensors, actuators, and energy storage systems. When a ferroelectric material is subjected to a cyclic electric field, the polarization response typically follows a characteristic hysteresis loop. This behaviour arises from the reorientation of domains, which are regions of aligned electric dipoles within the material.

Fig. 2.7 Polarization vs. electric field (PE) hysteresis loop tracer (Radient Inc.).

In this study, the ferroelectric hysteresis loops were measured using a Precision Ferroelectric Tester (e.g., Radiant Technologies Inc.) under ambient conditions (see Fig. 2.7). The polished disc-shaped samples were coated with silver electrodes to form parallel plate capacitors. The sample was connected to the tester using conductive leads. Afterwards, a bipolar triangular waveform with varying amplitude was applied across the sample. Finally, the polarization response was recorded and plotted as a function of the applied electric field. The electric field was incrementally increased to ensure accurate measurement of the saturation polarization and coercive field. The polarization-electric field (*P*–*E*) hysteresis loops provide valuable insights into the ferroelectric nature of the material [11]. The nature of ferroic ordering can be determined by analyzing the shape of the ferroelectric hysteresis loop, as illustrated in Fig. 2.8. Notably, a long-range ferroelectric structure exhibits a distinct, almost rectangular loop with significant remanent polarization. In contrast, relaxor ferroelectrics display a slender or narrow loop, indicative of weaker ferroelectric behavior.

Additionally, the area within the hysteresis loop corresponds to the energy dissipated during the polarization switching process. Due to their high remnant polarization, long-range ordered ferroelectrics possess well-defined polarization states, making them suitable for memory applications such as FeRAM. On the other hand, ferroelectrics with slim loops (relaxors) demonstrate low energy loss and high recoverable energy, highlighting their potential for use in ferroelectric energy storage devices.

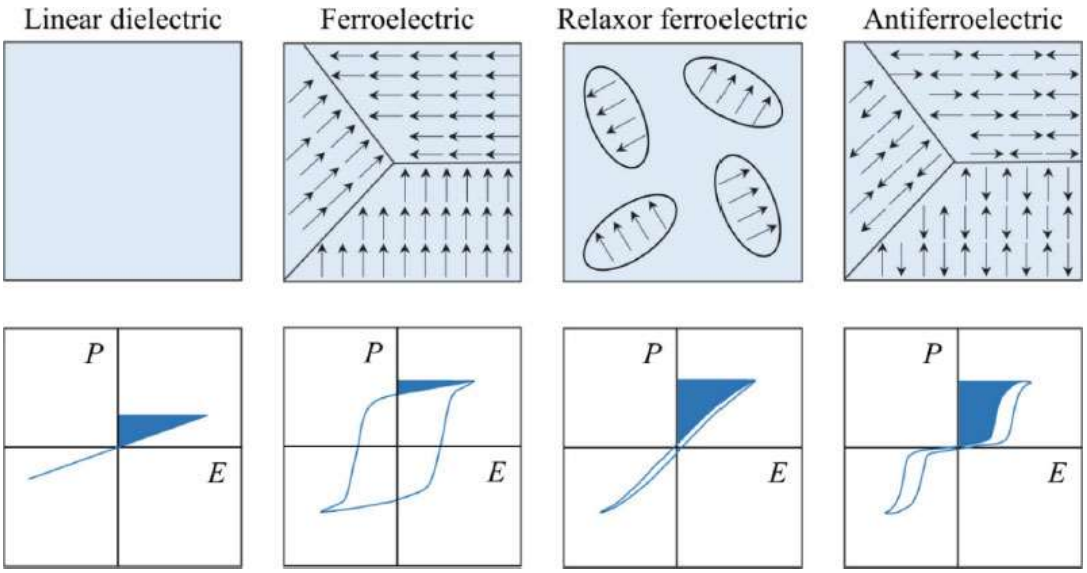

Fig. 2.8 Schematic illustration of dipoles, domain structures and polarization hysteresis loops for linear dielectrics, ferroelectrics, relaxor ferroelectrics and antiferroelectric materials. The figure is adopted from [11].

In conclusion, the measurement of polarization vs. electric field hysteresis loops is a vital technique for understanding the ferroelectric characteristics of materials. In the present study, sodium niobate-based ceramics NN-xBCT demonstrated a long-range ferroelectric or relaxor-like behaviour depending on the composition (x). The data obtained from these measurements provide essential insights into the type of ferroic ordering, which is valuable for defining their suitability for various technological applications.

2.2.7 Microstructural Measurement

Microstructural engineering is an effective way to tune the functional properties of ferroelectric materials [9]. The grain size plays a key role in influencing their dielectric and piezoelectric behaviour [228]. It can be controlled by manipulating the particle size of the starting powder or modifying the sintering process. Another useful method is domain engineering, which involves creating stable and optimized domain sizes to enhance functional properties. While this technique is commonly used in single crystals, it is less frequently applied to polycrystalline materials [9]. However, these approaches are interconnected since the grain size directly influences the domain size in polycrystalline materials. Optimizing the grain size typically enhances both small and large signal electromechanical properties, increases relative permittivity, lowers the Curie temperature, and reduces the coercive field compared to materials with non-optimized grain sizes [229]. The ideal grain size maximizes the density of switchable domain walls while minimizing back-switching. However, excessively large grains can degrade piezoelectric and dielectric properties due to significant back-switching [230]. On the other hand, very small grains often suppress ferroelectricity as reduced lattice distortion limits polarization [231]. Additionally, at extremely small grain sizes, domain stability can be compromised, with spontaneous polarization being neutralized by grain boundary charges or polarization gradients. As a result, each material has a specific threshold grain size below which ferroelectricity disappears.

Scanning Electron Microscopy (SEM) is a powerful imaging technique used to investigate the surface morphology and microstructural characteristics of polycrystalline materials. It provides high-resolution images by scanning the sample with a focused beam of electrons. The interaction of these electrons with the sample generates various signals, including secondary electrons, backscattered electrons, and characteristic X-rays, which carry valuable information about the sample's topography, composition, and crystallography. In the context of this work, SEM was used to analyze the microstructure of the

Fig. 2.9 High-resolution scanning electron microscope.

sintered sodium niobate-based ceramics. Understanding the microstructural features, such as grain size, grain boundaries, porosity, and phase distribution, is essential for establishing structure-property relationships. In this thesis work, the microstructural observations were performed using a high-resolution scanning electron microscope (HR-SEM: Nova Nano SEM 450, FEI Company of USA (S.E.A.) PTE, LTD) (shown in Fig.2.9). The obtained SEM images were analyzed to extract the surface morphology, grain size distribution, grain boundaries, porosity, densification, etc. of the synthesized ceramic samples.

2.3 Conclusion

This chapter focuses on the synthesis techniques and characterization methods employed in this thesis. The conventional solid-state reaction method was used for sample preparation, which is a simple and cost-effective method for preparing perovskite-based samples. Additionally, this chapter elaborates on the theoretical foundations of the various characterization techniques. The subsequent chapter explores the findings related to lead-free Sodium Niobate based smart materials.